Simulation and inversion of harmonic infrasound from open-vent volcanoes using an efficient quasi-1D crater model

Leighton M. Watson[a], Eric M. Dunham[a,b], Jeffrey B. Johnson[c]

[a]*Department of Geophysics, Stanford University, Stanford, California, United States*
[b]*Institute of Computational and Mathematical Engineering, Stanford University, Stanford, California, United States*
[c]*Department of Geosciences, Boise State University, Boise, Idaho, United States*

Abstract

Volcanic activity excites low frequency acoustic waves, termed infrasound, in the atmosphere. Infrasound observations can be used to provide constraints on eruption properties, such as crater geometry and volume flux. At open-vent volcanoes, such as Erebus (Antarctica) and Villarrica (Chile), the infrasound signal is modulated by the crater properties. Eruptive activity at the bottom of the crater, such as unsteady degassing or explosions, can excite the air mass within the crater into resonance leading to infrasound generation with signals possessing clear spectral peaks, termed harmonics. Therefore, the effect of the crater on the infrasound signal, or crater acoustic response, must be accounted for when inverting harmonic infrasound observations for eruption properties at open-vent volcanoes. Here we develop a linearized model of quasi-one-dimensional (1D) wave propagation inside volcanic crater coupled with 3D axisymmetric radiation into the atmosphere from the crater, with waves generated by a volumetric flow rate source at the bottom of the crater. We perform simulations for a range of volcanic crater geometries, temperature profiles, gas compositions, and source descriptions to explore the influence of these properties on the infrasound signal. The observed infrasound signal depends on the flow rate source-time function, but interference of up- and down-going waves within the crater selectively amplifies the signal at the resonant frequencies of the crater. The crater resonance model presented here is verified by comparison with an established three-dimensional (3D) infrasound code and is shown to be appropriate for realistic crater geometries when the crater radius is less than approximately one quarter of the acoustic wavelength. The model presented here is more computationally efficient and can be used to invert infrasound observations for a range of properties, such as crater geometry or volumetric flow rate associated with eruptions. We demonstrate the utility of our efficient modeling framework by inverting harmonic infrasound observations for the crater geometry and position of the lava lake at Villarrica volcano. This technique may be used at other open-vent volcanoes to constrain dynamic crater geometry and provide insights about lava lake motions and infrasound producing eruption sources.

Keywords: volcano infrasound, resonance, acoustic resonance, infrasound modeling

1. Introduction

Volcanic activity frequently generates acoustic waves in the atmosphere. Much of the energy is below the audible range of frequencies (Hagerty et al., 2000; Rowe et al., 2000; Johnson, 2003) and hence is termed infrasound. Infrasound signals are generated by nearly all types of activity (Fee and Matoza, 2013): passive degassing at Kilauea (Hawaii; Fee et al., 2010a), bubbles bursting at Stromboli (Italy; Ripepe et al., 1996; Vergniolle and Brandeis, 1996) and Erebus (Antarctica; Johnson et al., 2008; Gerst et al., 2013), explosive eruptions at Sakurajima (Japan; Ishihara, 1985; Johnson and Miller, 2014), and turbulence within erupted plumes at Tungurahua (Ecuador; Matoza et al., 2009; Fee et al., 2010b).

Harmonic infrasound signals, characterized by distinct peaks in the frequency domain, are observed at a number

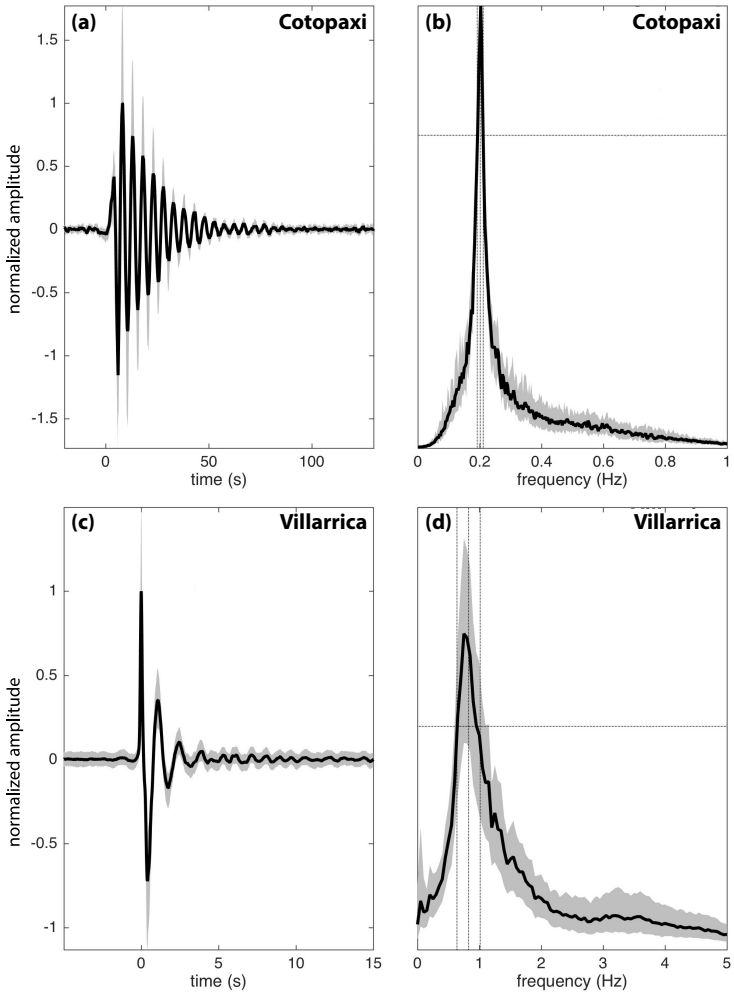

Figure 1: Harmonic infrasound signal in the time (left) and frequency (right) domains associated with discrete explosive events observed at Cotopaxi (top) and Villarrica (bottom). Grey lines are normalized explosion signals and black is the stack of all events. At Cotopaxi, 51 explosive events were recorded over 150 days in 2016. At Villarrica, 1000 explosive events were recorded on Feb 27, 2015.

of open-vent volcanoes including Cotopaxi (Ecuador; Johnson et al., 2018a), Etna (Italy; Spina et al., 2014), Kilauea (Garcés et al., 2003; Fee et al., 2010a) and Villarrica (Chile; Goto and Johnson, 2011; Richardson et al., 2014; Johnson et al., 2018b). Previous work has suggested that the harmonic nature of the observed infrasound signal is due to conduit processes (Ripepe et al., 2010) or due to resonance of the air mass within the crater, which can be further divided into Helmholtz resonance (Fee et al., 2010a; Goto and Johnson, 2011) and acoustic resonance (Richardson et al., 2014; Johnson et al., 2018b). Helmholtz resonance is the low frequency response of the air mass within the crater and occurs at wavelengths much longer than the characteristic depth of the crater such that the air mass within the crater can be described as a lumped parameter compressible object. Acoustic resonance occurs when acoustic wavelengths are comparable to the crater depth and waves are reflected within the crater to create standing waves.

In this work we develop a model for acoustic resonance within volcanic craters. Our model, which is appropriate for deep, narrow craters, computes the transfer function, termed the acoustic response, between an excitation source at the base of the crater and the response at remote infrasound stations. It describes the resonance of air within the crater as well as axisymmetric infrasound propagation from the crater outlet to the infrasound station. The model is limited to low amplitude eruptive activity as it assumes linear wave propagation.

Previous work has related the observed harmonic infrasound signal to crater properties using analytical expressions for the resonant frequencies (Fee et al., 2010a; Goto and Johnson, 2011; Richardson et al., 2014), however, this work has been limited to simple geometries. The model presented here is able to handle more general geometries, provided the crater is sufficiently deep and narrow, and hence is better able to describe realistic crater morphologies. Furthermore, our model is able to simulate the entire spectra of the infrasound signal, including fundamental frequencies and overtones, and the infrasound time series. This provides significantly important information that can be used to compare simulations results to data and to constrain inversions for crater properties.

Here we focus on acoustic resonance. We note that at some volcanoes, Helmholtz resonance may dominate at low frequencies with acoustic resonance only apparent at higher frequencies (e.g., Kilauea; Fee et al., 2010a). Conduit processes, such as recycling of degassed magma initiating gravity-driven oscillations in the conduit as proposed by Ripepe et al. (2010), may result in periodic excitation of acoustic waves. However, regardless of if the source process is periodic, the observed infrasound signal will still be influenced by acoustic resonance of the air mass within the crater.

A striking feature of many harmonic infrasound signals observed at volcanoes is that the fundamental mode dominates all other modes (Figure 1). In order for acoustic resonance to occur there are three conditions that must be met. Firstly, the crater radius must be small compared to the infrasound wavelength (i.e., $ka \ll 1$, where a is the crater radius and k is the wavenumber with $k = 2\pi/\lambda = 2\pi f/c$ where λ is the wavelength, f is the frequency, and c is the speed of sound) in order for there to be sufficient impedance contrast between the crater outlet and atmosphere to reflect acoustic waves back into the crater. If the crater radius is too large, relative to the acoustic wavelength, there will be a negligible impedance contrast at the crater outlet resulting in acoustic waves escaping to the atmosphere rather than resonating inside the crater. This provides an upper bound on the frequency of resonant modes as higher

frequency waves will be radiated to the atmosphere rather than trapped inside the crater. Secondly, the crater depth must be comparable to the wavelength with the exact relationship depending upon the geometry and impedance contrast at the outlet (for a cylindrical crater the longest possible wavelength is $\lambda \approx 4L$ where L is the crater depth). This provides a lower bound on the frequency as most volcanic craters have radii and depths on the order of ~100 m with deeper, narrower craters unsustainable as the crater wall rock will collapse. Thirdly, the realistic finite-duration sources have more energy at low frequencies and hence preferentially excite the fundamental mode. The combination of these three factors means that for volcanic craters there is generally only one resonant mode supported or at least only one mode with sufficient amplitude that it is observed in the data and hence the harmonic infrasound signal is often referred to as monotonic (e.g., Goto and Johnson, 2011) or monochromatic (e.g., Ripepe et al., 2010). In this manuscript we focus mainly on the fundamental resonant frequency that, for convenience, we refer to as the resonant frequency.

The modeling framework presented here is used to investigate how the harmonic infrasound signal depends upon the crater properties, including the geometry, temperature and gas composition, and the excitation source. Our simulations with axisymmetric radiation are compared to an established code that can describe arbitrary non-axisymmetric topography both inside and outside of the crater (infraFDTD; Kim and Lees, 2011). We examine Villarrica and Erebus volcanoes and assess the validity of our crater description and axisymmetric radiation model for approximating the solution with the real topography. Finally, we demonstrate how harmonic infrasound observations can be used to invert for crater geometry with an example from Villarrica volcano.

2. Model

We have developed a numerical model, referred to as CRes (Crater Resonance), that simulates the infrasound signal from open-vent volcanoes with axisymmetric craters and surrounding topography. The model has two components: 1.) an acoustic response function that depends upon the crater and atmospheric properties and describes the theoretical infrasound signal generated by an impulsive excitation at the base of the crater, and 2.) a description of the finite-duration source. Assuming linear wave propagation, the observed infrasound signal is the convolution, in the time domain, of the acoustic response function and the source:

$$\Delta p(t, r) = T(t, r) * s(t), \tag{1}$$

where Δp is the excess pressure or infrasound signal (Pa) recorded at a distance r from the crater outlet, T is the acoustic response function, and t is time. s is the source at the base of the crater and is expressed as a volumetric flow rate of air within the crater being pushed upwards, or pulled downwards, by the source process (m^3/s). As we are interested in examining the resonant modes and the frequency response of volcanic craters, the model is written in the frequency domain where the observed infrasound signal can be written as the product of the acoustic response function and source:

$$\Delta p(\omega, r) = T(\omega, r)s(\omega), \tag{2}$$

where ω is the angular frequency. Our modeling workflow is to start with a specified source function, $s(t)$, and take the Fourier transform to get $s(\omega)$. The infrasound signal in the frequency domain, $\Delta p(\omega, r)$, is then calculated by equation 2 and the inverse Fourier transform is used to obtain the infrasound signal in the time domain, $\Delta p(t, r)$.

The acoustic response function describes the theoretical infrasound signal generated by an impulse at the base of the crater. Our model involves three primary approximations, which are discussed in the following subsections: 1.) the quasi-1D crater description, 2.) the expression for terminating impedance at the crater outlet, and 3.) the atmosphere response model. These three approximations are all justified for $ka \ll 1$ and enable us to separate the acoustic response function into 1.) the crater acoustic response function, which describes wave propagation and resonant modes inside the volcanic crater, and 2.) the atmospheric response function, which describes acoustic radiation from the crater to the infrasound station. We note that some other studies (e.g., Johnson et al., 2018b) have used the term crater acoustic response to describe the transfer function from the source to the receiver. Here, we consider the crater acoustic response as the transfer function mapping the source at the base of the crater to the properties at the crater outlet, $z = 0$ where z is the vertical coordinate. The crater acoustic response, C, is defined as

$$C(\omega) = \frac{U(\omega, 0)}{s(\omega)}, \tag{3}$$

where U is the volumetric flow rate associated with acoustic waves. The atmosphere response function, P, is defined as

$$P(\omega, r) = \frac{\Delta p(\omega, r)}{U(\omega, 0)}, \tag{4}$$

allowing the acoustic response function, T, to be expressed as

$$T(\omega, r) = C(\omega)P(\omega, r) = \frac{U(\omega, 0)}{s(\omega)} \frac{\Delta p(\omega, r)}{U(\omega, 0)} = \frac{\Delta p(\omega, r)}{s(\omega)}. \tag{5}$$

2.1. Crater Acoustic Response Function

We model the crater as quasi-one-dimensional (allowing for changes in cross-sectional area with depth) and axisymmetric. This assumes that pressure is constant across cross-sections in the crater, which is valid for acoustic wavelengths that are long compared to the crater radius. Acoustic waves inside the crater are described by linear acoustics:

$$\frac{\partial U}{\partial t} + \frac{A}{\rho} \frac{\partial p}{\partial z} = 0, \tag{6}$$

$$\frac{\partial p}{\partial t} + \frac{K}{A} \frac{\partial U}{\partial z} = 0, \tag{7}$$

where p is the pressure and A is the cross-sectional area, which can vary as a function of depth . Gravity is negligible for this problem, both for the background state, as the crater depth is much less than the scale height of the atmosphere, and for acoustic perturbations, as compressibility restoring forces dominate gravitational restoring forces. The air inside the crater is described as an ideal gas with ambient density, ρ, and fluid bulk modulus, K, which is proportional to the ambient pressure for an ideal gas. Density and pressure are related by the ideal gas equation of state:

$$p = \rho RT, \tag{8}$$

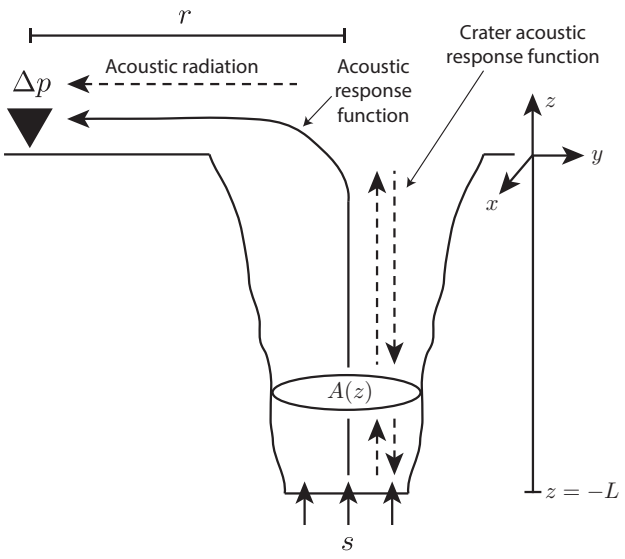

Figure 2: Schematic of model. The infrasound signal, Δp, observed at a distance r from the crater is related to the excitation source at the base of the crater, s, by the acoustic response function, T, which includes the crater acoustic response function that describes wave propagation inside the crater and associated resonant modes, and the atmosphere response function, which describes acoustic radiation from the crater outlet to the receiver.

where R is the specific gas constant and T is the temperature, not to be confused with response function T in equations (1) and (2). The speed of sound is

$$c = \sqrt{\gamma R T}, \tag{9}$$

where γ is the ratio of specific heats ($\gamma = 1.4$ for diatomic gases such as air).

We solve the governing equations in the frequency domain:

$$i\omega U + \frac{A}{\rho}\frac{\partial p}{\partial z} = 0, \tag{10}$$

$$i\omega p + \frac{K}{A}\frac{\partial U}{\partial z} = 0. \tag{11}$$

Equations 10 and 11 are solved using a summation-by-parts finite-difference discretization scheme (Del Rey Fernández et al., 2014; Svärd and Nordström, 2014). See Karlstrom and Dunham (2016) for more details on the numerical implementation. The model requires two boundary conditions, one at the bottom of the crater and one at the crater outlet. At the bottom of the crater, $z = -L$, the acoustic flow is specified as the source-time function:

$$U(t, -L) = s(t) = \iint_{A(L)} v(x, y, t)\, dx\, dy \tag{12}$$

where v is the vertical particle velocity (defined as positive upwards). A simple source model used by previous studies (e.g., Johnson et al., 2018b) is a Gaussian pulse:

$$s(t) = S \exp\Big(-\frac{1}{2}\frac{t^2}{\sigma^2}\Big), \tag{13}$$

where S is the amplitude of the pulse and σ controls the width.

At the outlet, $z = 0$, the pressure and acoustic flow are related by the terminating impedance, Z_T,

$$\frac{p(\omega, 0)}{U(\omega, 0)} = Z_T(\omega). \tag{14}$$

A constant pressure boundary condition could be applied could be applied at the outlet. However, this results in perfect reflection of acoustic waves. In order to allow acoustic waves to escape into the atmosphere and be recorded as infrasound, a more accurate description of the outlet is required. Here, we assume a flanged opening (Olson, 1957; Kinsler et al., 2000; Rossing and Fletcher, 2004) and the terminating impedance is given by (Rossing and Fletcher, 2004)

$$Z_T = R + iX, \tag{15}$$

where i indicates the imaginary unit, R is the acoustic resistance

$$R = Z_a\Big[\frac{(ka)^2}{2} - \frac{(ka)^4}{2^2 \cdot 3} + \frac{(ka)^6}{2^2 \cdot 3^2 \cdot 4} - \dots\Big], \tag{16}$$

and X is the acoustic reactance

$$X = \frac{Z_a}{\pi(ka)^2}\Big[\frac{(2ka)^3}{3} - \frac{(2ka)^5}{3^2 \cdot 5} + \frac{(2ka)^7}{3^2 \cdot 5^2 \cdot 7} - \dots\Big], \tag{17}$$

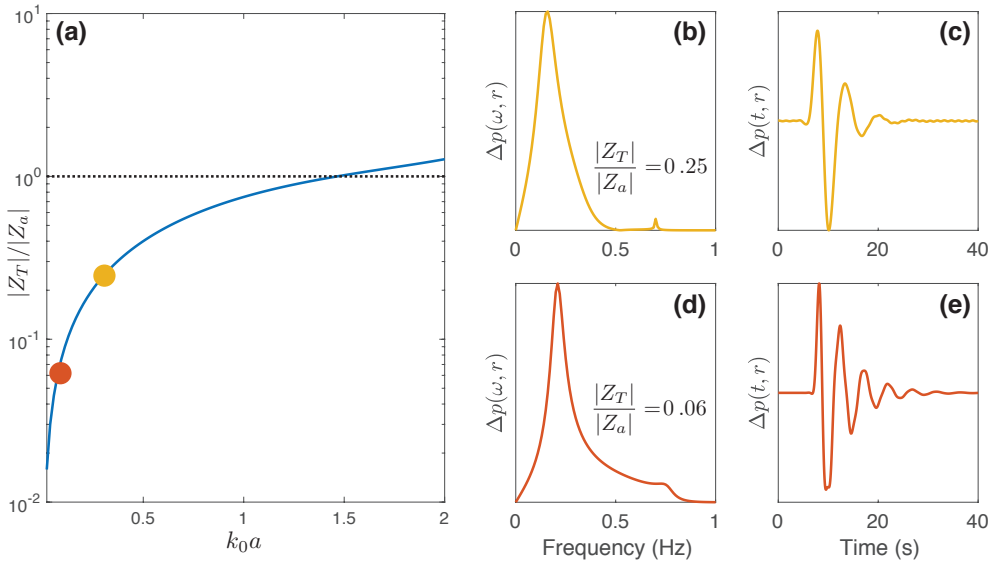

Figure 3: (a) Ratio of impedance contrast at crater outlet, $|Z_T|/|Z_a|$ as a function of dimensionless parameter ka evaluated at resonant frequency (k_0a). Synthetic infrasound signals calculated for a cylindrical pipe with a depth of 200 m and a radius of 200 m (b and c) and 400 m (d and e). Infrasound signals are excited by a Gaussian pulse with $\sigma = 0.4$ s. When the crater radius increases, ka and the impedance contrast between the crater and the atmosphere decrease allowing for more acoustic energy to escape to the atmosphere. This results in a broader peak in the frequency domain and a more rapidly damped signal in the time domain.

with k the wavenumber, a the crater radius at the outlet and $Z_a = \rho_a c_a / A(0)$ where ρ_a and c_a are the density and speed of sound in the atmosphere, respectively, and $A(0)$ is the cross-sectional area of the crater outlet. The observed infrasound signal is then calculated by multiplying the acoustic flow at the outlet with the atmosphere response function, as discussed in the following section.

The character of the infrasound signal depends upon the impedance contrast at the outlet, which depends upon the dimensionless parameter ka. If $ka \ll 1$ then there is a large impedance contrast and the outlet can be described as open with most of the wave energy reflected as if from a constant pressure boundary. This results in a narrow peak in the frequency domain and a slowly damped signal in the time domain. Conversely, if $ka > 1$ then the impedance contrast is lower and more of the wave energy is transmitted to the atmosphere, resulting in a broad peak in the frequency domain and a rapidly damped signal in the time domain (Olson, 1957; Rossing and Fletcher, 2004).

2.2. *Atmospheric Response Function*

We describe propagation of the infrasound signal from the crater outlet to the receiver as axisymmetric radiation from a baffled piston embedded in an infinite plane. The mapping from the outlet acoustic flow, $U(\omega, z = 0)$, to the excess pressure, $\Delta p(\omega, r)$, is given by (Rossing and Fletcher, 2004):

$$\Delta p(\omega, r) = i\omega \exp(-ikr) \frac{\rho_a a^2}{2r} \left[\frac{2J_1(ka \sin\theta)}{ka \sin\theta} \right] \frac{U(\omega, 0)}{\pi a^2}, \tag{18}$$

where J_1 is a Bessel function of order one, θ is the angle between the negative $z-$axis and the receiver (e.g., $\theta = \pi/2$ for a receiver located on the plane perpendicular to crater orientation), ρ_a is the density of the atmosphere, and a is the crater radius at the outlet. The baffled piston model reduces to the commonly used monopole source description (Woulff and McGetchin, 1976; Johnson and Miller, 2014) for radiation in a half-space in the low frequency limit when $ka \ll 1$,

$$\Delta p(\omega, r) = i\omega \exp(-ikr)\frac{\rho_a a^2}{2r}\frac{U(\omega, 0)}{\pi a^2}. \tag{19}$$

Here we do not account for topographic scattering. Later in the manuscript we compare our simulations with infraFDTD, a 3D linear acoustics wave propagation code that incorporates realistic topography (Kim and Lees, 2011), for Erebus and Villarrica volcanoes. In this work we are focused on the crater acoustic response function and hence, for simplicity, we use an axisymmetric atmospheric response function that assumes flat or dipping (section 5) topography. However, at some volcanoes, while the crater is sufficiently deep and narrow that the quasi-1D assumption used here is warranted, the surrounding topography outside of the crater is too complex to be approximated as axisymmetric. Nonetheless, the framework described above can still be used to model the infrasound signal at these volcanoes. This can be done by first calculating the crater acoustic response function using the method outlined in section 2.1. The atmospheric response function can then be calculated using a 3D code that accounts for topographic scattering, such as infraFDTD (Kim and Lees, 2011), assuming a source at the crater outlet (taken from the output of the crater acoustic response model) but otherwise not including the crater geometry. Multiplying the crater acoustic response function with atmospheric response function enables the acoustic response function to be calculated (equation 5) and hence the infrasound signal to be simulated (equation 2).

3. Verification and Benchmarking

We compare our model, CRes, with analytical solutions for cylindrical geometries and with axisymmetric solutions from a three-dimensional (3D) numerical model, infraFDTD (Kim and Lees, 2011) in order to test the decomposition of the acoustic response function into the product of the crater acoustic and atmosphere response functions. We demonstrate that CRes performs well for craters wider than the theoretical limit of $ka \ll 1$. CRes is in good agreement with infraFDTD up to $ka = O(1)$, demonstrating that the model presented here has utility for real volcano geometries such as Villarrica, which has a crater radius of 100 m, dominant infrasound frequency of ~1 Hz, and hence $k_0 a = 1.8$, where k_0 indicates the wavenumber evaluated at the resonant frequency (Johnson et al., 2018b).

3.1. Analytical Verification

The CRes numerical model is compared with analytical solutions for an idealized cylindrical crater. For a cylindrical crater that is open at the outlet (constant pressure at outlet) and closed at the base, which is a simple approximation to volcanic craters and the low frequency limit of equation 15, the resonant frequency of the fundamental mode is given by (Rossing and Fletcher, 2004):

$$f_0 = \frac{c}{4L}, \tag{20}$$

where f_0 is the resonant frequency, c is the speed of sound in the crater, and L is the depth of the crater. The derivation of this solution assumes that $ka \ll 1$, which is a valid assumption for long narrow pipes. However, at most volcanoes the crater radius and depth are of the same order and hence the assumption of $ka \ll 1$ used in deriving equation 20 is invalid. When the crater radius is a significant fraction of the depth air outside the crater can participate in the resonant oscillations. This means that the oscillating body of air has a greater length than the depth of the crater and hence a lower resonant frequency given by (Kinsler et al., 2000; Rossing and Fletcher, 2004; Vidal et al., 2006):

$$f_0 = \frac{c}{4L_{\text{eff}}} \text{ where } L_{\text{eff}} = L + \frac{8a}{3\pi}. \tag{21}$$

CRes accounts for the end-effects (air outside the crater being involved in the resonant oscillation) through the acoustic reactance (equation 17) in the expression for the terminating impedance (equation 15). The resonant frequency predicted by CRes and equation 21 are in good agreement for deep craters. However, at shallow depths $ka \to O(1)$ and the high order terms in the acoustic reactance become important, resulting in the two solutions diverging (Figure 4). The correction in equation 21 can be viewed as the first order correction for end-effects that is valid at low frequencies whereas the expression for acoustic reactance used by CRes is a more general description of end-effects.

3.2. Numerical Benchmarking

We also benchmark CRes through comparison with infraFDTD (Kim and Lees, 2011), a three-dimensional code that has been used in volcano infrasound studies (Kim and Lees, 2014; Kim et al., 2015; Fee et al., 2017). infraFDTD

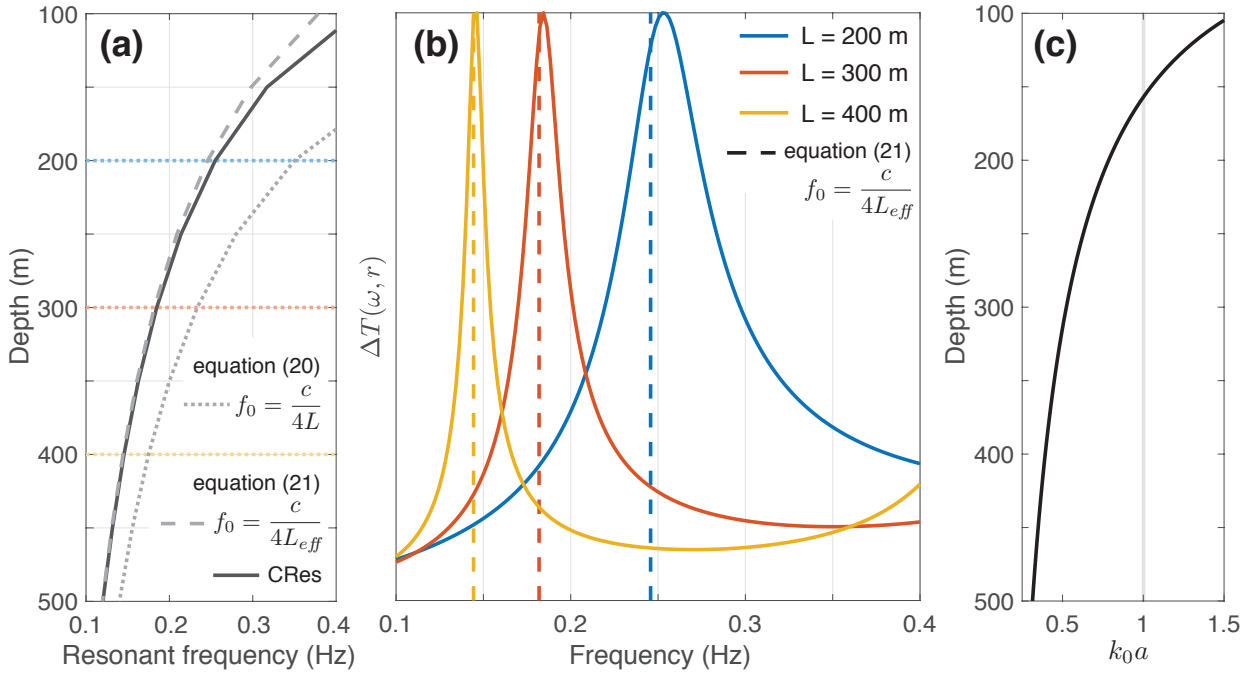

Figure 4: Comparison of resonant frequency for a cylindrical crater with a radius of 100 m as calculated by CRes (solid) and using equation 20 (dotted) and equation 21 (dashed). (a) Resonant frequency as a function of crater depth. (b) Normalized amplitude spectra of the acoustic transfer function, $T(\omega, r)$, for three different crater depths. The vertical dashed line indicates solution from equation 21. (c) dimensionless parameter ka evaluated at resonant frequency ($k_0 a$) as a function of depth. When the crater is deep the assumption that $k_0 a \ll 1$ is valid and CRes and equation 21 are in good agreement. When the crater is shallow $k_0 a \to 1$, the validity of the analytical solutions break down and, as a result, the solutions diverge.

is a finite-difference time-domain wave propagation code that solves the linear acoustics governing equations for a source function provided in terms of mass flux. The code assumes a rigid boundary between the atmosphere and solid earth.

Using both codes, we simulate the infrasound signal for an axisymmetric crater with a conical horn shape embedded in a flat plane. The crater has an inlet radius (at the bottom of the crater) of 10 m, an outlet radius of 100 m, and a depth of 200 m. The air both inside and outside the crater has a constant density of 1.22 kg/m^3 and a speed of sound of 340 m/s. The acoustic source is a Gaussian volume flux at the base of the crater with $\sigma = 0.4$. The infrasound signal is computed at a distance of 200 m from the center of the crater. The two different numerical models give almost identical results with resonant frequency of 0.5 Hz, which corresponds to a wavelength of 680 m and $k_0 a = 0.9$ (Figure 5). This demonstrates that the quasi-1D crater resonance approximation can be useful even when $ka = O(1)$. It is noted that, even though the station is close (100 m) to the crater rim, the two models give similar results. This suggests that diffraction of acoustic waves from the crater rim, (e.g., Kim and Lees, 2011; Lacanna and Ripepe, 2013), which is accounted for by infraFDTD, is unimportant for this geometry.

We also consider a wider crater and increase the crater radius from 100 m to 200 m. The acoustic source and atmospheric properties are unchanged. For the wider crater, the two models give different results. CRes under-predicts

the peak amplitude by 26%, over-predicts the resonant frequency by 14%, and has less energy at high frequencies. The resonant frequency from infraFDTD is approximately 0.4 Hz, which corresponds to a wavelength of 850 m and $k_0 a = 1.5$, and therefore some discrepancies between the two models are expected. CRes assumes that wavefronts are planar within the crater, an assumption that breaks down for wide craters with $ka = O(1)$, whereas infraFDTD can describe curved wavefronts.

We note that CRes retains most of the features seen in the infraFDTD simulation results and is substantially computationally cheaper, although we note that infraFDTD runs efficiently on a standard GPU processor without the need for high performance computing resources. For the simulations presented in Figure 5, CRes uses 200 grid points inside the crater and is solved in < 1 s whereas infraFDTD takes ~250 s to compute the solution on $\sim 1 \times 10^7$ grid points.

The results presented here suggest that CRes has utility at volcanoes with wide shallow craters where $ka = O(1)$. It could be used for preliminary analysis or to obtain a starting point for a more expensive 3D inversion. It is noted that we have so far restricted our analysis to axisymmetric geometries. In section 6 we compare CRes and infraFDTD for realistic crater geometries at Villarrica and Erebus volcanoes.

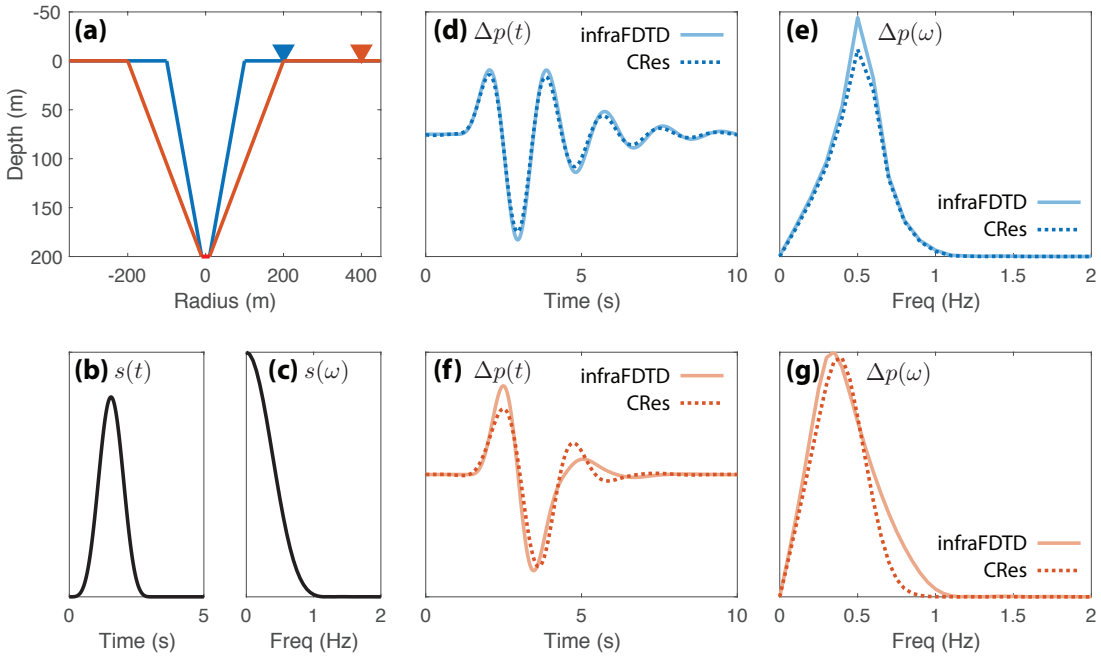

Figure 5: Infrasound signal calculated by the quasi-1D crater resonance model presented here, CRes (dotted), assuming axisymmetric radiation and using the 3D code, infraFDTD (solid), for two different axisymmetric crater geometries. (a) Crater geometry and station location with 2.5x vertical exaggeration. (b) and (c) Acoustic flow at base of crater in the time and frequency domains, respectively. (d) and (e) show the synthetic infrasound signal for the narrow crater while (f) and (g) show the signal for the wide crater. The solutions CRes and infraFDTD are in good agreement for the narrow crater ($k_0 a = 0.9$) but diverge for the wider crater ($k_0 a = 1.5$).

4. Sensitivity of Harmonic Infrasound Signal to Crater Properties

Here, we investigate the sensitivity of the infrasound signal to several crater properties, namely crater geometry and sound speed, which is influenced by temperature and gas composition. The acoustic response function is strongly influenced by the crater geometry and is only weakly dependent on the temperature and gas composition through their influence on the speed of sound. The infrasound signal also depends upon the source or volumetric flow rate at the base of the crater. We consider a range of possible source models and examine how the source influences the infrasound signal.

4.1. Geometry

The shape of volcanic craters is of significant interest to volcanologists and observatory staff because monitoring how geometry changes over time can lend insight to eruption dynamics. At volcanoes with lava lakes, the position of the magma surface is of particular interest and varies over the shortest time scale, except during crater collapse. During the 2018 eruption of Kilauea the summit lava lake drained more than 300 m in 10 days (Neal. et al., 2019). Estimating crater geometry and lava lake position can be challenging, especially at many of the persistently degassing volcanoes that display harmonic infrasound signals, as visual observations are hampered by gas emissions and access to the vent area is hazardous. Therefore, the prospect of estimating crater geometry from remote observations is attractive.

The crater geometry is one of the primary controls on the harmonic infrasound signal. For a cylinder, this is illustrated by equation 20 where resonant frequency of the fundamental mode is inversely proportional to the pipe length. Simple analytical expressions relating the geometry to the infrasound do not exist for more complex geometries and, in some cases, the resonant frequency can vary non-monotonically with depth (e.g., Johnson et al., 2018a).

The geometry also influences the width of the peak in the amplitude spectra and the rate of amplitude decay in the time series. This is related to the amount of damping in the system and is quantified by the quality factor (Rossing and Fletcher, 2004):

$$Q = \frac{f_0}{\Delta f}, \tag{22}$$

where Q is the quality factor, f_0 is the resonant frequency, and Δf is the frequency difference between the low and high corner frequencies, which are where the amplitude spectrum drops to $1/\sqrt{2}$ of the amplitude at f_0. The quality factor is inversely proportional to the amount of damping or attenuation that is present in the system. A high quality factor corresponds to low attenuation and a narrow peak in the frequency domain whereas a low quality factor corresponds to substantial attenuation and a broad peak in the frequency domain. In our model attenuation is solely due to radiative losses. We do not include any intrinsic attenuation mechanisms. The quality factor can be used to calculate the exponential decay constant, α, of the signal envelope in the time domain (Rossing and Fletcher, 2004):

$$\alpha = \frac{\pi f_0}{Q}. \tag{23}$$

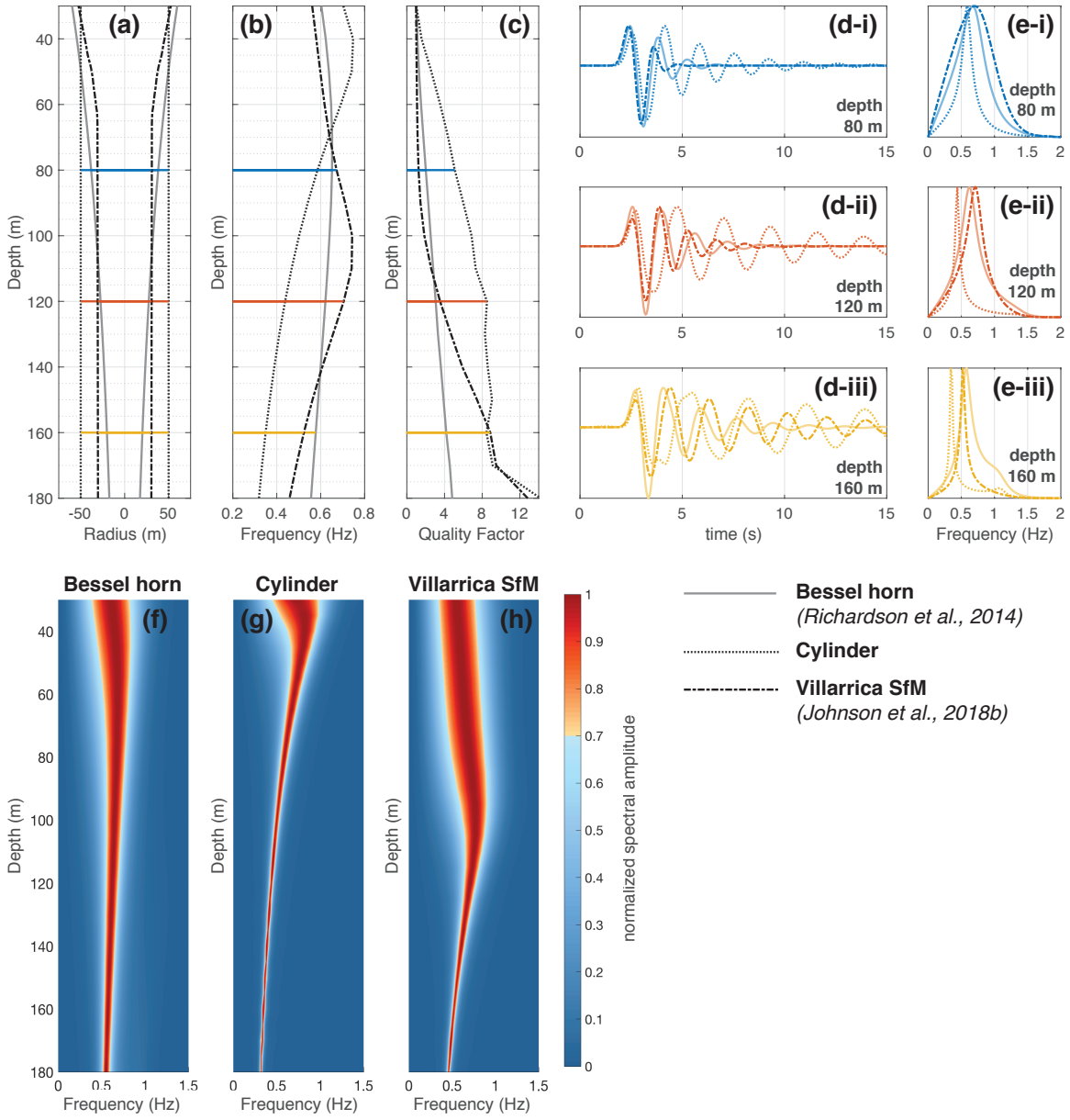

Figure 6: Simulated infrasound signal as a function of depth for three different crater geometries. (a) Bessel horn geometry used by Richardson et al. (2014) to approximate Villarrica Volcano, Chile (solid), a cylinder (dotted) and the Villarrica geometry constructed with structure-from-motion (SfM) that was used by Johnson et al. (2018b) (dashed-dotted). The different crater geometries produce substantially different infrasound signals. Crater geometries are shown with 3.7x vertical exaggeration. (b) Resonant frequency and (c) quality factor as a function of depth. Infrasound signal in the (d) time and (e) frequency domains for crater depths of (i) 80 m, (ii) 120 m, and (iii) 160 m are shown. Amplitude spectra for (f) Bessel horn geometry of Richardson et al. (2014), (g) cylindrical crater, and (h) Villarrica geometry of Johnson et al. (2018b). Amplitude spectra are normalized at each depth slice. The color change from blue to red corresponds to the corner frequencies in the amplitude spectra (where amplitude spectra drops to $1/\sqrt{2}$ of the peak amplitude). Acoustic waves are excited by a Gaussian pulse with $\sigma = 0.3$ s at the base of the crater.

A high quality factor results in a low value of α and means that the signal in the time domain oscillates for an extended period of time. When the radius of the crater is increased there is less of an impedance contrast at the crater outlet. Therefore, it is easier to radiate energy. This results in a low quality factor and a broader peak (Figure 3). Conversely, a narrow crater has a high impedance contrast at the outlet, which means that acoustic waves are preferentially reflected from the crater outlet rather than radiated into the atmosphere. This results in a high quality factor and a narrow peak.

We simulate the infrasound signal for three different crater geometries as a function of depth (Figure 6) using an acoustic source described by a Gaussian volume flux with $\sigma = 0.3$ s (equation 13) occurring at the base of the crater. The infrasound signal is strongly modulated by the different crater geometries. For a depth of 120 m, depending on the geometry, the resonant frequency can be anywhere between 0.4 and 0.7 Hz while the quality factor varies between 3 and 8.5. The model presented here extends previous work on acoustic resonance of volcanic craters (e.g., Richardson et al., 2014) as we are able to simulate the infrasound signal for axisymmetric crater profiles with $ka < 1$ rather than being limited to analytical horn geometries.

Of note, the resonant frequency for all three geometries does not decrease monotonically with increasing depth. Therefore, using the frequency to invert for the crater depth, such as done by Richardson et al. (2014), may result in a non-unique crater depth solution. Full characterization of the infrasound spectra using CRes thus provides additional information, such as the quality factor, which can be used to provide more constraints on the crater geometry (Johnson et al., 2018b).

4.2. Speed of Sound

The acoustic response and resultant infrasound radiation are also influenced by the speed of sound in the crater. This is clearly illustrated for a cylinder where the resonant frequency is related to the travel-time of an acoustic wave. We consider temperature profile and gas composition inside the crater as two possible controls on the sound speed. We determine that while the harmonic infrasound signal does depend upon the temperature and gas composition, reasonable variations in these parameters provide a smaller influence than variations in the crater geometry.

4.2.1. Temperature

The air temperature inside a volcanic crater can vary significantly between volcanoes. Fee et al. (2010a) used FLIR imagery to estimate the average air temperature inside Halema'uma'u crater at 200°C while Oppenheimer and Kyle (2008) performed FTIR spectroscopy of gas emissions at Erebus and calculated an air temperature of 125°C inside the crater. In addition, the air temperature within a crater is spatially variable. For example, at Erebus the average atmospheric temperature is −25°C whereas the lava lake surface temperature ranges from 500°C to 1000°C (Calkins et al., 2008; Oppenheimer and Kyle, 2008; Gerst et al., 2013).

Here, we consider several different temperature profiles inside a crater. For modeling simplicity, we consider a cylindrical crater that is 200 m deep with a radius of 100 m. Acoustic waves are excited by a Gaussian volume flux with $\sigma = 0.3$ s at the base of the crater. The temperature of the atmospheric air outside of the crater is 0°C with

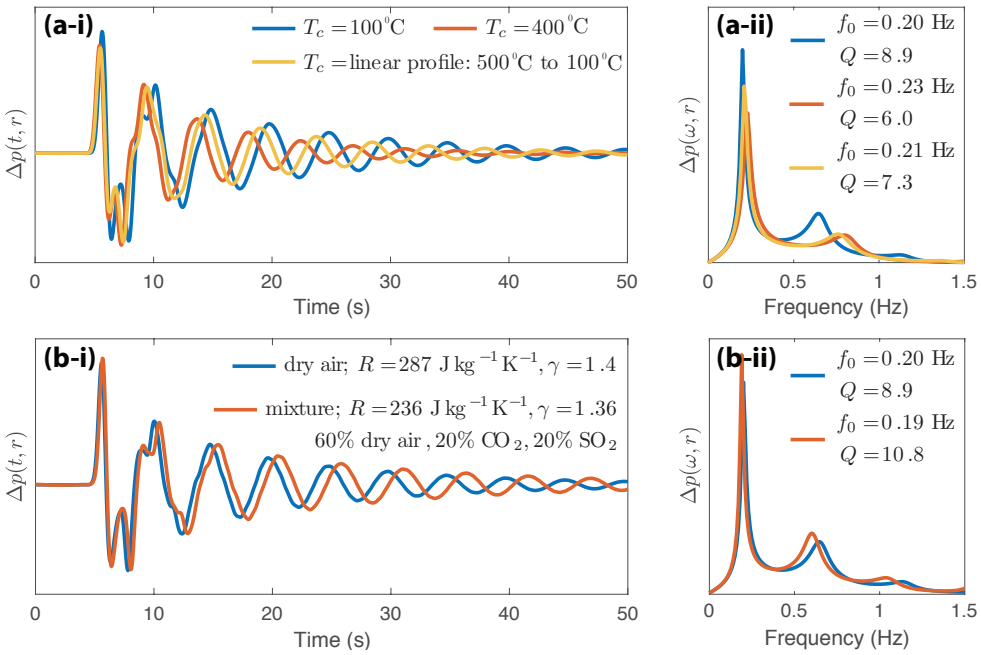

Figure 7: Simulated infrasound signal, Δp, for a pipe of 100 m radius and 200 m depth for a range of (a) crater temperatures and (b) gas compositions. Acoustic waves are excited by a Gaussian pulse with σ = 0.3 s at the base of the crater

a density of 1 kg/m^3. The background pressure is assumed constant in the atmosphere and crater. This allows us to calculate the air density within the crater based on the ideal gas law (equation 8). We consider three temperature profiles within the crater: (1) a cool crater with a constant profile of 100°C, (2) a hot crater with a constant profile of 400°C, and (3) a linearly varying temperature profile from 500°C at the base of the crater to 100°C at the outlet.

Figure 7a shows the simulated infrasound signal in the time and frequency domains for the different temperature profiles. The resonant frequency of the hotter (faster speed of sound) crater is higher, as expected. Increasing the crater temperature from 100°C to 400°C causes the resonant frequency to increase from 0.2 Hz to 0.23 Hz and the quality factor to decrease from 8.9 to 6.0. The reduced quality factor indicates that the hotter crater has a reduced impedance contrast with the atmosphere and is more readily able to radiate acoustic energy.

4.2.2. Gas Composition

The speed of sound can also be influenced by the gas composition. The gas composition is described by the specific gas constant, R, and ratio of heat capacities, γ, which are varied here in another sensitivity analysis. The specific gas constant and ratio of heat capacities can be significantly lower if substantial quantities of volcanic gases such as CO_2 (R = 189 J kg^{-1} K^{-1}, γ = 1.289) or SO_2 (R = 130 J kg^{-1} K^{-1}, γ = 1.29) are present. Here, we consider end member compositions of dry air (R = 287 J kg^{-1} K^{-1}, γ = 1.4) and a mixture of 60% dry air, 20% CO_2 and 20% SO_2 (R = 236 J kg^{-1} K^{-1}, γ = 1.36).

We again consider a 200 m deep cylindrical crater with a radius of 100 m and acoustic waves excited by a Gaussian

volume flux with σ = 0.3 s at the bottom of the crater. The temperature is 0°C in the atmosphere and 100°C inside the crater. The speed of sound is proportional to the square root of the product of the specific gas constant and ratio of heat capacities (equation 9). Decreasing the specific gas constant, which occurs when high molar mass volcanic gases such as CO_2 and SO_2 are present, results in a lower sound speed (c = 387 m/s for dry air versus c = 345 m/s for the mixture) and hence a lower resonant frequency (reduced from 0.20 Hz to 0.19 Hz, Figure 7b). Decreasing the specific gas constant increases the quality factor (from 8.9 for dry air to 10.8 for the mixture). The quality factor depends upon the impedance contrast at the outlet, which is influenced by the gas composition through the effect of the speed of sound on k in the expression for the terminating impedance (equation 15).

In summary, decreasing the specific gas constant decreases the speed of sound, which increases the impedance contrast at the outlet leading to trapped acoustic energy and higher quality factor. Gas composition can influence the speed of sound in the crater, but reasonable variations in gas species appear to lead to only a 10% reduction in sound speed. Given that this influence is small, and also that it is particularly hard to accurately measure crater gases, we continue the sensitivity analyses using dry air with R = 287 J kg^{-1} K^{-1} and γ = 1.4.

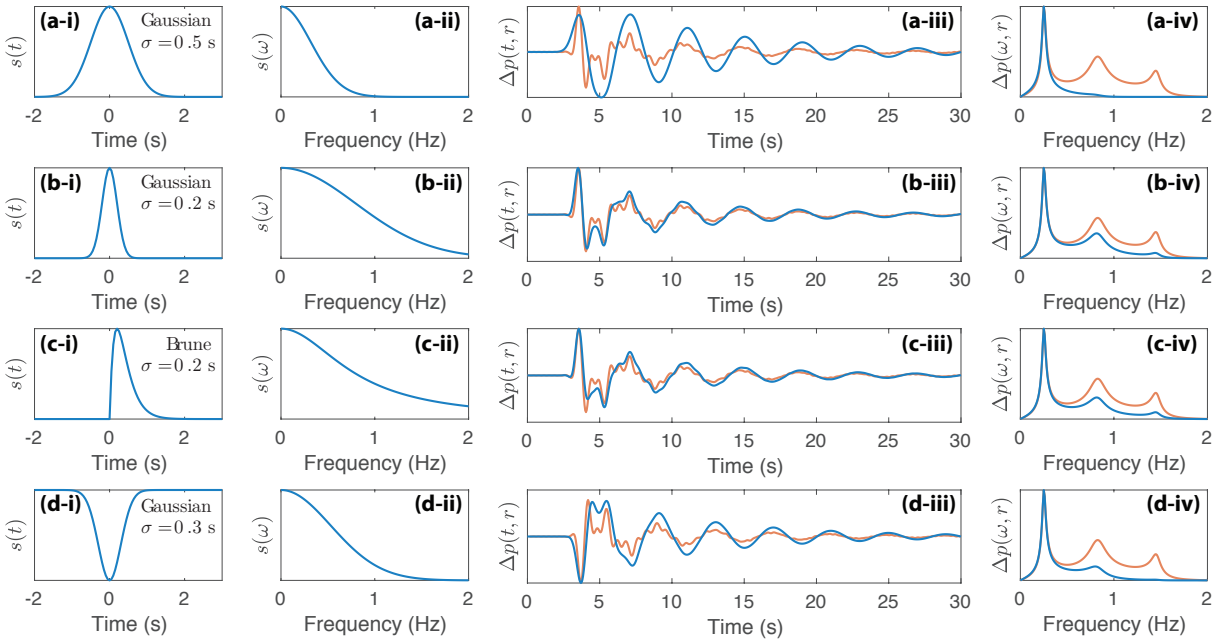

Figure 8: Simulated infrasound signal for a cylindrical crater with a radius of 100 m and a depth of 200 m for four different source descriptions (a-d). The source is specified in terms of a volumetric flow rate at the base of the crater, which is shown in both the time (i) and frequency (ii) domains. (iii) and (iv) show the infrasound signal, Δp (blue), and the acoustic response function, T, (red) in the time and frequency domains, respectively. Note that for (d) the acoustic response function has been multiplied by −1. The more impulsive sources generate infrasound signals that are very similar to the acoustic response function. The longer duration sources only excite energy at low frequencies and the corresponding infrasound signal is a low-pass filtered version of the acoustic response function.

4.3. Source

There are many processes at open-vent volcanoes that can excite acoustic waves including bursting gas slugs (Vergniolle et al., 1996; Gerst et al., 2013; Witsil and Johnson, 2018), unsteady degassing (Fee et al., 2010a; Goto and Johnson, 2011) and crater floor collapse (Johnson et al., 2018a). In CRes acoustic waves are excited by the volumetric flow rate at the base of the crater. Here, we explore the influence of different volumetric flow source-time functions on the infrasound signal, which is the convolution of the acoustic response function with the excitation source (equation 1).

The convolution of the acoustic response function with the source acts as a low-pass filter on the acoustic response function; low frequencies are relatively unchanged but there is reduced signal at higher frequencies because a finite duration source only generates excitation over a limited frequency range. A short impulsive source, such as a bubble rapidly bursting, excites energy over a wider range of frequencies and in this case the infrasound signal may be similar to the acoustic response function. On the other hand, a long duration source, such as due to a slow variation in degassing rates, excites energy only at low frequencies and the infrasound signal will only contain the low frequency components of the acoustic response function.

We previously considered a Gaussian source description (equation 13). This is probably the simplest possible source description and has been used by previous studies (e.g., Johnson et al., 2018b). However, radar observations of the velocity of bursting bubble surfaces (Gerst et al., 2013) and full-waveform inversion results using numerical Green's functions (Kim et al., 2015) suggest that the volumetric flow rate may have a more rapid onset followed by a slower decay, which is better described by the Brune model (Brune, 1970):

$$s(t) = S\,tH(t)\exp\left(-\frac{t}{\sigma}\right), \tag{24}$$

where S is the amplitude, σ controls the width and $H(t)$ is the Heaviside function.

The observed infrasound signal from open-vent volcanoes, where the acoustic source is deep inside the crater, can be heavily modulated by the crater geometry (Figure 8), as has been explored by several previous studies (e.g., Richardson et al., 2014; Johnson et al., 2018a,b). Therefore, understanding how the crater can influence the infrasound signal is important for interpreting harmonic infrasound observations.

5. Acoustic radiation from conical volcanoes

In many volcano infrasound studies (e.g., Johnson and Miller, 2014; Kim et al., 2012; Yamada et al., 2017) acoustic radiation into the atmosphere is approximated as radiation into a half space bounded at the bottom by the earth's surface. However, many volcanoes have steep topography and the assumption of radiation into a half-space is simplifying (e.g., Kim et al., 2015; Fee et al., 2017). Here, we articulate a correction to account for radiation from a conical volcanic edifice (Johnson et al., 2012).

In the time domain, the pressure due to a point source volume flux, or monopole source, radiated out to a whole space can be written as (Lighthill, 1978):

$$\Delta p(t, r) = \frac{\rho \ddot{V}(t - r/c)}{4\pi r}, \tag{25}$$

where $\ddot{V}$ is the rate of change of volume flux and c is the wave speed. The factor 4π is a geometric factor due to radiation into a whole space and $1/r$ is the amplitude decay from geometric spreading. However, Earth's surface reflects acoustic waves and restricts the domain to a smaller volume. A simple correction for radiation in half space is

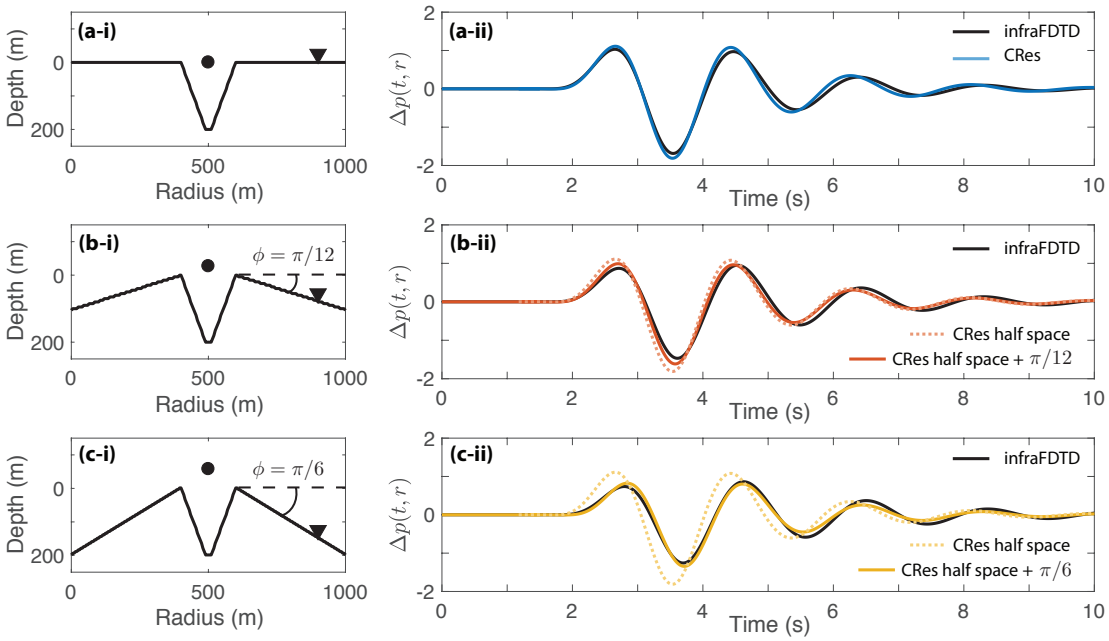

Figure 9: Radiation from a conical volcano. Comparison between infraFDTD 3D simulations (black, solid) and CRes model for radiation into a half space (equation 26, colored, dashed) and from a conical volcano (equation 27, colored, solid). We perform simulations for three different volcano geometries: (a) a crater terminating in a flat plane, in which case $\phi = 0$ and equation 26 and equation 27 give the same result, (b) ground surface sloping away from the crater at 15° ($\phi = \pi/12$) and (c) at 30° ($\phi = \pi/6$). Crater profiles are plotted with 1.3x vertical exaggeration. For equation 27, r is measured from the apex of the conical volcano (circle) to the receiver (triangle). For volcano geometries where the ground surface slopes down from the crater the model of radiation from a conical volcano (equation 27) gives a closer match in amplitude and arrival time to the 3D solution than the model of radiation into a half space (equation 26).

to half the geometric factor in equation 25 (e.g., Johnson and Miller, 2014):

$$\Delta p(t, r) = \frac{\rho \ddot{V}(t - r/c)}{2\pi r}. \tag{26}$$

This is the time domain form of equation 19 and is rigorously justified based on the baffled piston description (equation 18) in the limit that $ka \ll 1$. In the case of radiation from the apex of a conical volcano the sound radiates into a medium that is in between the half-space and whole-space end members. Suppose ϕ is the dip angle from the horizontal to the sloping ground surface ($\phi \in [0,\ \pi/2]$) then radiation into the larger space can be described by:

$$\Delta p(t, r) = \frac{\rho \ddot{V}(t - r/c)}{(2\pi + 4\phi) r}, \tag{27}$$

where $(2\pi + 4\phi)$ is the solid angle. Increased solid angle implies a diminished pressure for the same acoustic source. In the limit that $\phi = \pi/2$ equation 27 retrieves the expression for radiation into a whole space (equation 25). Furthermore, it is important to recall that r is the slant distance from the apex of the volcanic cone to the receiver rather than the horizontal distance from the center of the crater to the receiver. The effect of radiation from a conical volcano can be included in the baffled piston radiation model (equation 18) by replacing the 2π in the denominator with $2\pi + 4\phi$.

We perform 3D simulations using infraFDTD for three different slope angles and take these results as the true solution. These results are compared to CRes for radiation into a half space (equation 26) and radiation from a conical volcano (equation 27). Equation 26 over predicts the amplitude by 50% and under predicts the arrival time of the peak by 5% (peak amplitude of 1.11 Pa and peak time of 2.65 s for a volcano edifice dipping at an angle of 30° compared to the 3D simulation values of 0.74 Pa and 2.79 s). Using equation 27, which accounts for radiation into a larger solid angle and the slant distance, we obtain a better fit (over predict peak amplitude by 10% and over predict arrival time by 2%) to the true solution (Figure 9), which demonstrates the utility of this simple correction to the acoustic radiation model, especially at volcanoes with pronounced slopes.

6. Realistic volcano crater geometries

In this section, we compare simulations for realistic volcano geometries using both CRes and infraFDTD (Kim and Lees, 2011). For many volcano geometries, the crater radius is about the same order of magnitude as the crater depth. The quasi-1D crater resonance model, CRes, requires the assumption of long wavelengths relative to the crater radius and the point at which this assumption gives rise to misfit was investigated in section 3. Here we demonstrate that CRes is able to capture most of the spectral features produced in the infraFDTD simulations, which incorporate complex topography. CRes is also able to describe the amplitude and shape of the initial peak in the infrasound time series.

We consider two volcanoes, Villarrica (Chile) and Erebus (Antarctica), with two different crater shapes and aspect ratios. Villarrica has a narrower crater and there is good agreement for the infrasound signal between the CRes and infraFDTD simulations. Erebus has a wider crater and CRes, while able to accurately model the amplitude and shape of initial peak in the time series, is unable to capture the later oscillations, or coda, which are caused by reflection and scattering of acoustic waves from the crater walls.

6.1. *Villarrica*

Villarrica is a basaltic-andesitic volcano in the southern Andes that has a long-lived active lava lake at the base of the crater (Witter et al., 2004; Richardson et al., 2014). The general state of activity of Villarrica is persistent out-gassing and mild eruptions ranging from seething magma to strombolian bubble bursts (Witter et al., 2004; Palma et al., 2008; Richardson et al., 2014), although this background level of activity is punctuated by paroxysmal eruptions every few decades, most recently in 1985 and 2015 (Van Daele et al., 2014; Johnson and Palma, 2015).

The crater of Villarrica has a radius of ~100 m at the outlet and slopes downwards from the rim for about 50 m

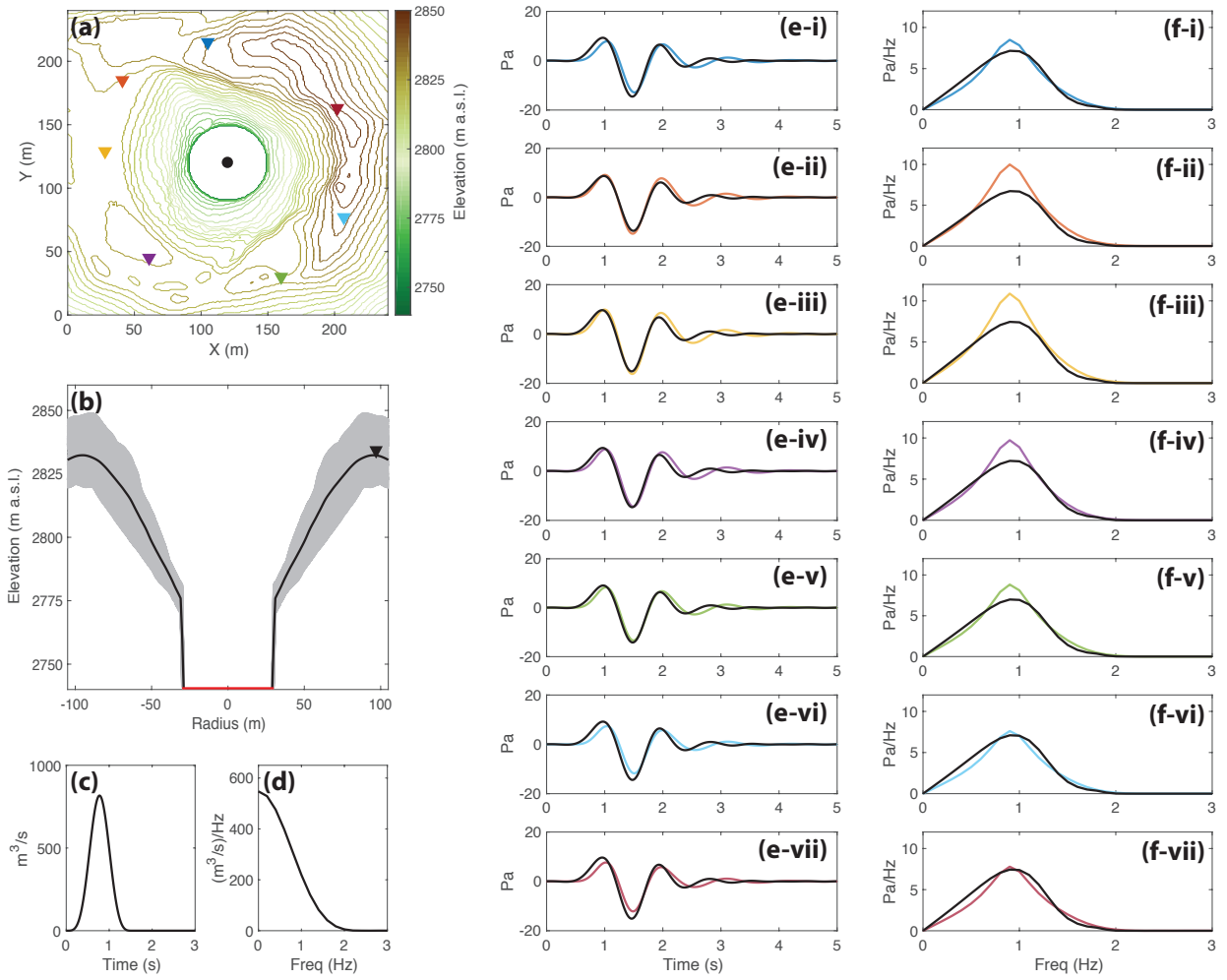

Figure 10: Comparison of CRes and infraFDTD simulations for Villarrica volcano demonstrating that for Villarrica's ~100 m wide crater CRes provides a reasonable approximation to the 3D solution using infraFDTD. (a) DEM of Villarrica (Johnson et al., 2018b) showing station locations (colored triangles) and acoustic source position (black circle). (b) Axisymmetric crater geometry (black) with 1.7x vertical exaggeration obtained by averaging radial slices through the DEM (grey). (c) and (d) show the volumetric flow rate at the base of the crater, *s*, in the time and frequency domains, respectively. (e) and (f) Synthetic infrasound signal in the time and frequency domains, respectively, for CRes (black) and infraFDTD (colored). The color corresponds to the station position shown in (a).

before continuing as a vertical walled shaft down to the active lava lake surface. The digital elevation model (DEM) used here is constructed from aerial images using the imaging processing technique structure-from-motion. More than a thousand images were acquired from $\sim$ 500 m above the summit and used to construct an orthomosaic image and DEM with 1 m resolution (Johnson et al., 2018b). Reconstruction was considered accurate down to the point where the upper crater flare transitions to a vertical-walled shaft.

We simulate the acoustic response and infrasound signal for Villarrica volcano using both the CRes and infraFDTD codes (Figure 10). In CRes the simulated infrasound is excited by a Gaussian volumetric flux at the base of the crater as discussed in section 2.1. In infraFDTD the volumetric flux is localized as a point source in the center of the crater. The two models produce similar synthetics for Villarrica's geometry. Despite the crater radius and depth being of comparable size, CRes captures much of the complexity of the infrasound waveform, including its coda oscillations and the amplitude and shape of the initial peak of the infrasound time series. Peak amplitudes from CRes are on average within 9% of those from infraFDTD and arrival times are within 5%. We note that there are differences between the models for the infrasound time series coda. This is likely because the later arrivals included reflected and scattered waves that are not described by CRes or because of diffraction of acoustic waves at the crater rim (Kim and Lees, 2011; Lacanna and Ripepe, 2013).

Theoretically, the 1D approximation is valid in the limit at $ka \ll 1$. For the geometry of Villarrica used here we have a crater outlet radius of $\sim$100 m, a resonant frequency of $\sim$1 Hz and assumed sound speed of 340 m/s. This gives $ka \approx 1.8$, which clearly violates that assumption that $ka \ll 1$. Nonetheless, the simulations presented here demonstrate that CRes can be used to simulate harmonic infrasound observations at Villarrica and, by extension, at other volcanoes with craters with similar dimensions.

6.2. *Erebus*

Erebus is a 3794 m high stratovolcano located on Ross Island, Antarctica. The summit crater has a radius of 150 m and a depth of ~200 m with an active lava lake, Ray Lake, located at the bottom of the crater. Despite the remote location, Erebus has been well monitored with a telemetered network seismic, infrasound and video data (Rowe et al., 2000; Aster et al., 2004).

Acoustic waves are excited by pressurized gas slugs rising through the magma column and bursting at the surface of the lava lake. Infrasound observations at Erebus are characterized by a clear initial peak followed by a smaller

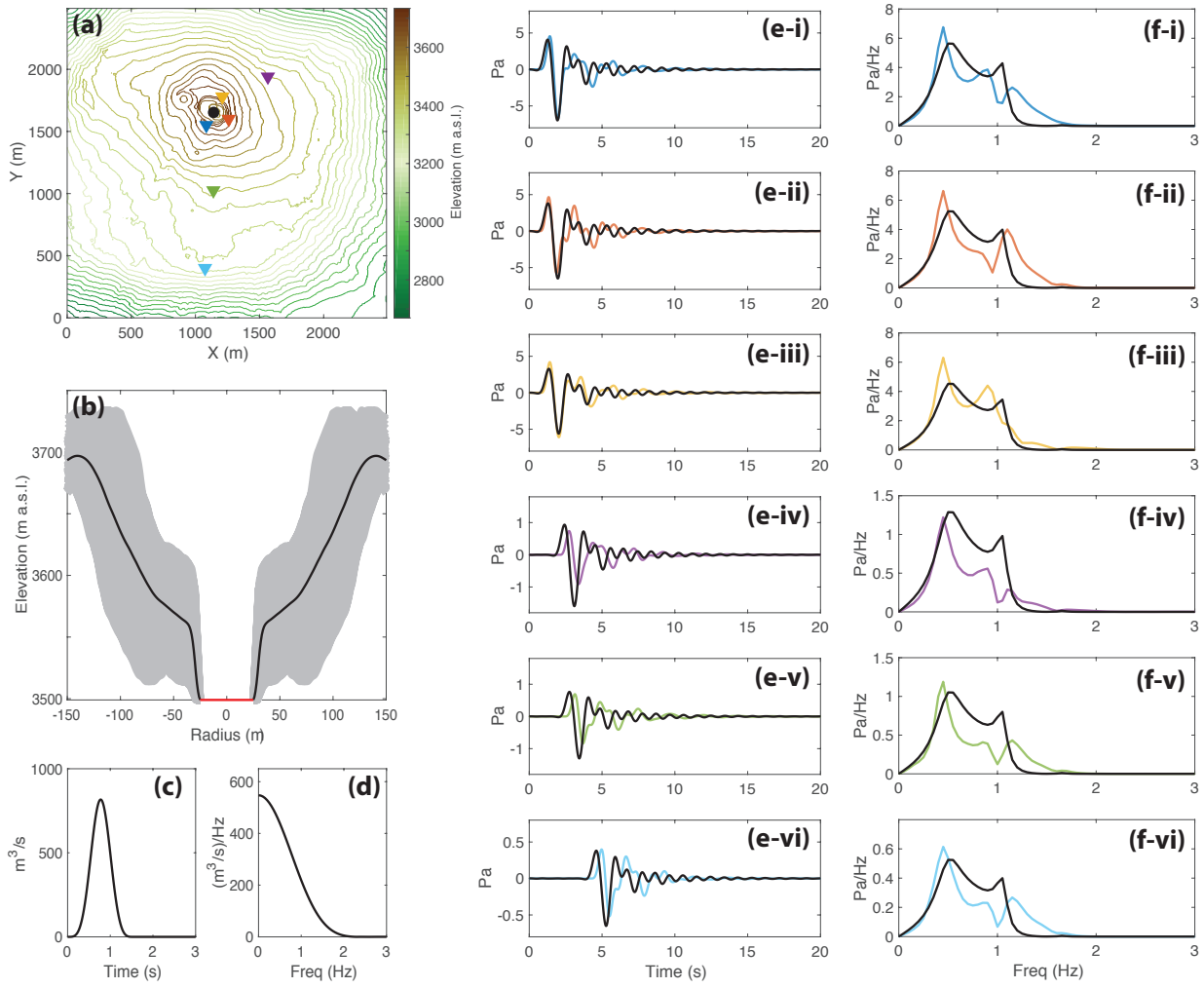

Figure 11: Comparison of CRes and infraFDTD simulations for Erebus volcano. (a) DEM of Erebus (Csatho et al., 2005) showing station locations (colored triangles) and acoustic source position (black circle). (b) Axisymmetric crater geometry (black) with 1.2x vertical exaggeration obtained by averaging radial slices through the DEM (grey). (c) and (d) show the volumetric flow rate at the base of the crater, s, in the time and frequency domains, respectively. (e) and (f) Synthetic infrasound signal in the time and frequency domains, respectively, for CRes (black) and infraFDTD (colored). The color corresponds to the station position shown in (a).

amplitude coda and multiple spectral peaks that are thought to be due to scattering from the steep crater walls (Witsil and Johnson, 2018).

We compare simulation results from CRes and infraFDTD applied to the Erebus geometry (Figure 11). CRes is mostly able to match the amplitude and shape of the initial peak of the infrasound time series. Peak amplitudes are on average within 15% of those from infraFDTD. CRes, however, is unable to describe the complexity of the coda seen in the infraFDTD as these later arrivals are influenced by topographic scattering, which is directionally variable for the non-axisymmetric Erebus crater geometry. In the frequency domain, the two codes display similar trends with both predicting multiple spectral peaks, but at different frequencies; CRes gives two peaks at 0.5 Hz and 1 Hz whereas infraFDTD gives two or three peaks, depending on the station location, at 0.45, 0.9 and 1.1 Hz. In addition to topographic scattering, CRes only describes resonance in the crater in the vertical direction whereas infraFDTD can describe resonance due to waves propagating horizontally in the crater, which can be an important component of the signal for wide craters like at Erebus and Kilauea (Fee et al., 2010a). These simulations argue that while the quasi-1D crater resonance model presented here is appropriate for modeling the initial transient and relating properties of the bursting bubbles to the infrasound signal, a 3D model, such as infraFDTD, is required to examine the later coda oscillations that are influenced by topographically scattered waves.

Witsil and Johnson (2018) compared visual and infrasound observations of bubbles bursting at the surface of Ray Lake and were able to relate the initial infrasonic transient to the bursting of the bubble and discovered that the bursting source was not directly related to the coda. They argued that the coda was due to the reflection of acoustic waves from the craters walls (see Kim et al. (2015) who also examined topographic scattering of acoustic waves) and therefore not directly related to their visual observations of bubble bursts. This is supported by our modeling that shows a good match between the results from CRes and infraFDTD for the initial peak but discrepancies for the coda. Nonetheless, Figure 11 demonstrates that the quasi-1D crater resonance model, CRes, can be used to provide an approximate description of the harmonic infrasound signal even at volcanoes with wide craters, such as Erebus. CRes is computationally efficient and can be used as part of inversions to estimate crater geometry as discussed in the next section.

7. Inverting harmonic infrasound observations for crater properties

Given the suitability of CRes for modeling infrasound for several synthetic and realistic crater geometries, we now explore how the model can be used to invert infrasound data to recover crater properties. We consider harmonic infrasound observations from Villarrica volcano (Chile) in the days prior to the paroxysmal eruption of 3 March 2015 when the lava lake stage was changing and causing the effective length of the crater to change over time (Johnson et al., 2018b). Infrasound data were recorded by a network of stations, but we use data from station VID (6.4 km to the west of the vent) as this had the best signal-to-noise recordings during the lead-up to the eruption. The infrasound data were continuously recorded using 24-bit loggers at 100 Hz and identical MEMS-based transducers (Marcillo et al., 2012), which possess a flat frequency response between 0.04 Hz and a 50 Hz Nyquist frequency. The data are filtered above 0.5 Hz to remove contamination from microbaroms. For more information on station geometry and data acquisition see Johnson et al. (2018b).

The infrasound signal changed in the days prior to the paroxysmal eruption with the resonant frequency increasing and quality factor decreasing. Johnson et al. (2018b) hypothesized that the change in the infrasound was due to the lava lake rising in the crater and used peak frequency and quality factor information to invert for the lava lake position assuming a constant crater geometry constrained in the upper crater by structure-from-motion observations. Here, we focus on an inversion of the characteristic infrasound spectra recorded on two different days when the lava lake was thought to be at low and high stands. We invert for crater geometry, which shows that while crater shape remained largely unchanged the variations in spectra can be explained by the lava lake ascending in the crater. This further supports the hypothesis of Johnson et al. (2018b) and demonstrates the utility of infrasound monitoring of open-vent volcanoes and the power of the model presented here.

We formulate the inverse problem in the frequency domain and define the misfit function, M, as

$$M = \beta_f \frac{|f_0^d - f_0^s|}{f_0^d} + \beta_Q \frac{|Q^d - Q^s|}{Q^d}, \tag{28}$$

where f_0^d and f_0^s are the resonant frequencies of the data and simulations and Q^d and Q^s are the quality factor of the data and simulations, respectively. β_f and β_Q are weighting factors that determine how the inversion scheme prioritizes fitting the resonant frequency versus quality factor.

We solve the inverse problem using a Monte-Carlo Markov-Chain (MCMC) style scheme. We define $\boldsymbol{x}$ as a vector of model parameters and begin the inversion from an initial estimate $\boldsymbol{x}_0$. For each iteration of the inversion a proposed set of parameters values, $\boldsymbol{x}^*$, are computed by taking a random step in each of the parameter values. For the ith iteration the proposed solution is given by

$$\boldsymbol{x}_i^* = \frac{\boldsymbol{x}_{i-1}}{\boldsymbol{x}_0} + \boldsymbol{h}_{i-1}\Delta x \tag{29}$$

where $\boldsymbol{h}_{i-1}$ is a vector that is the same size as $\boldsymbol{x}$ with each entry randomly sampled from the uniform distribution $[-1, 1]$ for each iteration and Δx is the scalar step size. The parameter values are normalized by the initial estimate so that the maximum step size is equal percentage-wise in each parameter direction.

For each proposed solution, $\boldsymbol{x}_i^*$, CRes is used to simulate the amplitude spectra and the resonant frequency and quality factor are computed. The misfit for the proposed solution, M_i^* is computed and the proposed solution is accepted ($\boldsymbol{x}_i = \boldsymbol{x}_i^*$) if:

1. the misfit is reduced, $M_i^* < M_{i-1}$, or
2. $\gamma < a$, where γ is a random number sampled from the uniform distribution $[0, 1]$ and a is a scalar parameter, $a \in [0, 1]$. This condition allows a certain number of points to be accepted even if the misfit increases rather than decreases. This allows the inversion scheme to escape local minima.

If neither of these conditions are met then the proposed solution is discarded and a new $\boldsymbol{x}_i^*$ is computed. The process repeats until a proposed solution is accepted and a new iteration begins. The inversion is stopped after a specified number of iterations.

The inversion framework also allows the source and gas properties to be inverted for. However, in this manuscript we assumed fixed values for the gas properties ($T = 100$°C and $Q = 287$ J kg^{-1} K^{-1}) and only invert for the crater geometry. The source is a Brune pulse with a duration of $\sigma = 0.3$ s. We note that we only consider normalized amplitudes. Future work could consider amplitude information, which may allow harmonic infrasound observations to be inverted for total volumetric flow rate and provide constrains on emitted gas volume.

Acoustic radiation is the only source of attenuation in our model. In reality there are more damping mechanisms and hence we choose $\beta_f > \beta_Q$, which prioritizes fitting the resonant frequency over the quality factor. We have performed inversions for a range of β_f and β_Q and for all choices, provided the inversion converges, the crater geometry is similar, which gives us confidence in the results. For the results shown here we chose $\beta_f = 3$ and $\beta_Q = 1$. We use a maximum step size of $\Delta x = 0.01$ as, after multiple trials of different values, this choice provides a balance between a large step size that enables escape from local minima and a small step size that allows close convergence to the global minima. Future work could utilize a variable step size that decreases as the misfit decreases. We chose $a = 0.9$, which means that there is a 10% chance that guesses that increase the misfit will be accepted. This provides a balance between iterations decreasing the misfit function and allowing the inversion scheme to escape local minima.

We parameterize the crater geometry as a depth and N radii values that are equally spaced in depth. The depth of the kth radii value at the *ith* iteration is given by:

$$z_i^k = (k-1)\frac{L_i}{N-1}, \tag{30}$$

where L_i is the crater depth at the ith iteration and $k \in [1, \ldots, N]$. The depth is evolved with each iteration and as a result the depth of the radii values also change. The crater radius is linearly interpolated between the specified radii values. For the results shown here we chose $N = 5$ and hence the specified radii values are located at depths of $[0,\ L_i/4,\ L_i/2,\ 3L_i/4,\ L_i]$. The initial estimates of parameter values, $\boldsymbol{x}_0$ are given by

$$\boldsymbol{x}_0 = [r_0^1, r_0^2, r_0^3, r_0^4, r_0^5, L_0], \tag{31}$$

where r_0^k are the initial estimates of the radial values at the kth depths given by equation 30 and L_0 is the initial estimate of the crater depth.

We examine infrasound data recorded at Villarrica volcano on two days, 26 February and 1 March, during the period prior to the paroxysmal eruption of 3 March 2015. Infrasound signals are excited by discrete short-duration explosions and are characterized by an impulsive compressional pulse followed by a rarefaction and sinusoidal coda decaying over several seconds (Figure 1). In the frequency domain, the signals display a single harmonic (monotonic) peak (Johnson et al., 2018b). For our inversion, we consider the stacked explosion waveform recorded over a day at station VID.

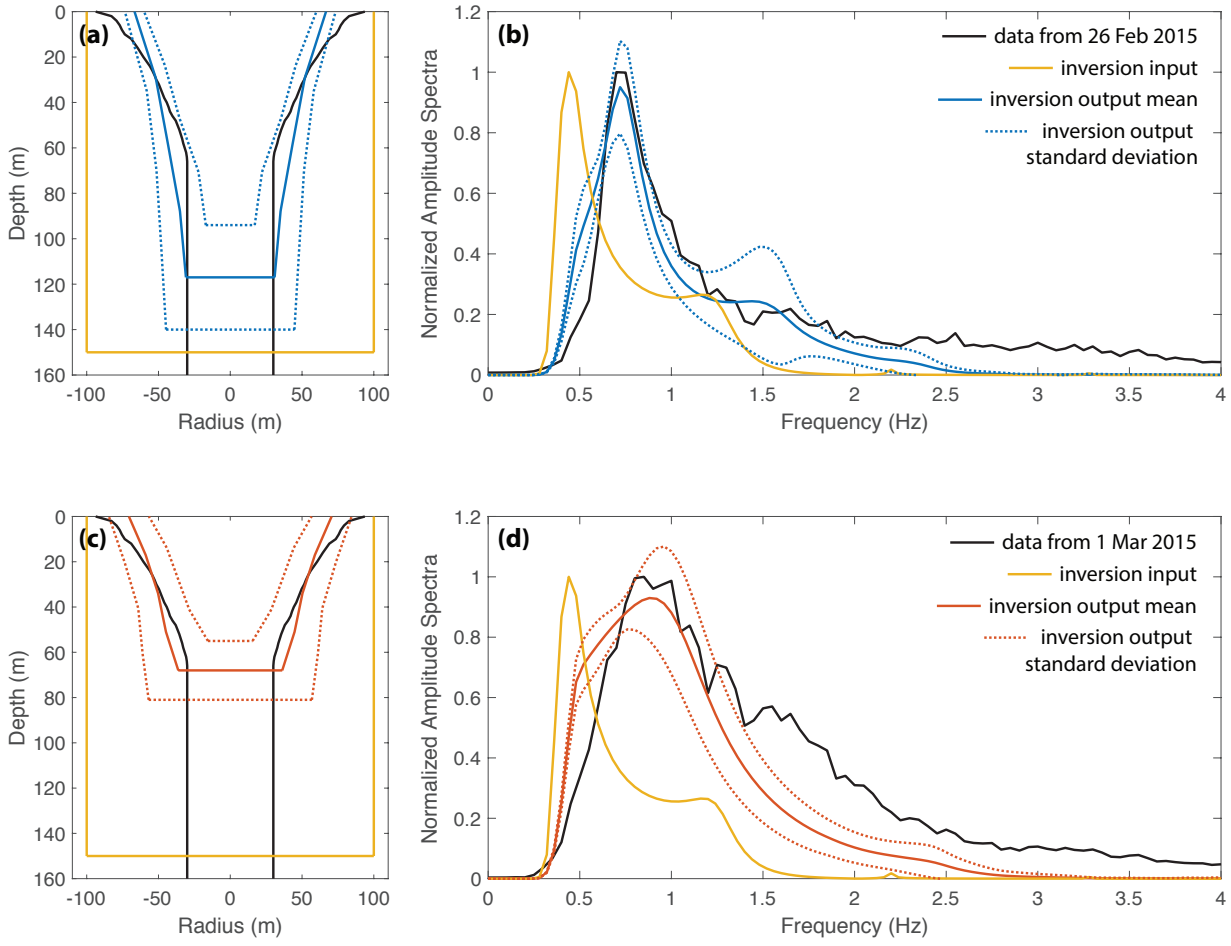

Figure 12: Inversion of infrasound data for crater geometry at Villarrica volcano on (a and b) 26 Feb 2015 and (c and d) 1 Mar 2015. (a and c) Crater geometry. The black line shows the crater geometry that Johnson et al. (2018b) estimated from visual observations of Villarrica using structure-from-motion while the yellow line indicates the initial estimate of the crater geometry that is input to the inversion scheme. The solid (a, blue; c, red) lines indicates the mean output crater geometry and the dashed lines show one standard deviation. (b and d) Data and simulations of normalized infrasound amplitude spectra. The data and simulations are both filtered above 0.5 Hz to remove contamination in the data from microbaroms. Data represent daily averaged values for 1,000 events (ie., ~40 per hour).

		Input	Output	Data
26 Feb	f_0 (Hz)	0.36	0.72	0.72
	Q	4.03	3.17	3.39
1 Mar	f_0 (Hz)	0.36	0.81	0.88
	Q	4.03	1.16	1.44

Table 1: Resonant frequency and quality factor of infrasound data and simulations at Villarrica volcano. The inversion output is in good agreement with the data and is a substantial improvement on the inversion input.

We initialize our inversion with a cylindrical crater with a radius of $r_0^k = 100$ m for $k = 1, ..., 5$, which is approximately equal to the crater radius observed at the surface, and a depth of $L_0 = 200$ m. The simulated spectra for the cylindrical geometry is a poor match to the observed data (Figure 12) and the resonant frequency and quality factor are substantially different to the data (Table 1). However, after 10,000 iterations (removing the first 10% to reduce the sensitivity to initial conditions) the simulated spectra for the mean crater geometry approaches that of the data. The mean output resonant frequency and quality factor of the simulations, as desired by the inversion scheme, are in good agreement with the data. Furthermore, the output geometry is in good agreement with visual estimates of Villarrica's crater geometry (Johnson et al., 2018b). The crater shapes are similar for both times and the depth is shallower on 1 March (mean depth of 68 m compared to 117 m on 26 February). This supports the conclusions of Johnson et al. (2018b) who showed that the changes in resonant frequency and quality factor of the infrasound observations reflected the ascent of the lava lake at Villarrica prior to the 3 March paroxysm.

We note that the data has greater amplitudes at high frequencies than the simulations. This is likely because there are high frequency signals captured by the infrasound receivers that are not included in the simulations such as wind noise.

The inversion results presented here demonstrate how harmonic infrasound observations can be inverted for crater geometry at open-vent volcanoes. As infrasound measurements can be recorded continuously and at safe distances, this technique has substantial utility in tracking how crater geometry and eruption properties evolve through time, which can shed insight onto eruption dynamics.

A similar inversion scheme to the method presented here can be used to efficiently invert for an unknown crater geometry when the topography surrounding the crater is known but is too complex to be approximated as axisymmetric. Due to the assumption of linear wave propagation, the crater acoustic and atmospheric response functions can be calculated separately (equation 5). Rather than assuming axisymmetric radiation into a half space, the atmospheric response function can be computed using a 3D code, such as infraFDTD, that accounts for topographic scattering for an impulsive source at the crater outlet and otherwise not accounting for the crater geometry. As before, the crater acoustic response function can be computed using the quasi-1D model discussed in section 2.1. The inversion of observed infrasound data for crater geometry can be performed as outlined in this section with the exception that instead of using equation 26 to propagate the infrasound signal from the crater outlet to the receiver the previously calculated

3D atmospheric response function is used. This inversion will be of similar computational efficiency despite using a more complex atmospheric propagation model because the atmospheric response function only has to be computed once.

8. Conclusion

Harmonic infrasound signals are observed at a number of open-vent volcanoes and are due to excitation of the air mass, which resonates within the crater. The observed infrasound signal is a heavily modulated version of the source-time function and depends upon the crater properties, primarily the crater geometry. We show that while the infrasound signal does depend upon the temperature and gas composition inside the crater, reasonable variables in these parameters provide a smaller influence than variations in the crater geometry. By analyzing the harmonic infrasound recorded at distant sites information about both the crater shape and eruption mechanisms can be recovered.

Previous work using analytical models is insufficient for characterizing the crater acoustic response adequately for more complex, morphologically realistic crater shapes. This work shows that a numerical quasi-1D crater resonance model is adequate for recovering good crater response functions for realistic volcano geometries and that these can be used to invert for crater geometries. Furthermore, by simulating the entire amplitude spectra and time series, rather than just solving for the resonant frequency, the model presented here, CRes, provides significantly more information that can be used to constrain inversions of the infrasound data. CRes is most appropriate for deep, narrow craters but the results presented here demonstrate that the model has substantial utility for a range of realistic volcano geometries. This work shows the importance of accounting for the crater acoustic response when analyzing infrasound data, especially at open-vent volcanoes where the acoustic source is deep within the crater, and demonstrates the utility of infrasound monitoring, including inverting for crater geometry and tracking changes during eruptive activity, at open-vent volcanoes that produce harmonic infrasound signals.

References

Aster, R., McIntosh, W., Kyle, P., Esser, R., Bartel, B., Dunbar, N., Johns, B., Johnson, J., Karstens, R., Kurnik, C., McGowan, M., McNamara, S., Meertens, C., Pauly, B., Richmond, M., Ruiz, M., 2004. Real-time data received from mount erebus volcano, Antarctica. Eos 85 (10).

Brune, J. N., 1970. Tectonic stress and the spectra of seismic shear waves from earthquakes. Journal of Geophysical Research 75 (26), 4997–5009.

Calkins, J., Oppenheimer, C., Kyle, P. R., 2008. Ground-based thermal imaging of lava lakes at Erebus volcano, Antarctica. Journal of Volcanology and Geothermal Research 177 (3), 695–704.

Csatho, B., Schenk, T., Krabill, B., Wilson, T., Lyons, W. B., McKenzie, G., Hallam, C., Manizade, S., Paulsen, T., 2005. Airborne Laser Scanning for High- Resolution Mapping of Antarctica. Eos, Transactions, American Geophysical Union 86 (25), 237–238.

Del Rey Fernández, D. C., Hicken, J. E., Zingg, D. W., 2014. Review of summation-by-parts operators with simultaneous approximation terms for the numerical solution of partial differential equations. Computers and Fluids 95, 171–196.

Fee, D., Garcés, M., Patrick, M., Chouet, B., Dawson, P., Swanson, D., 2010a. Infrasonic harmonic tremor and degassing bursts from Halema'uma'u Crater, Kilauea Volcano, Hawaii. Journal of Geophysical Research 115 (B11), B11316.

Fee, D., Garces, M., Steffke, A., 2010b. Infrasound from Tungurahua Volcano 2006-2008: Strombolian to Plinian eruptive activity. Journal of Volcanology and Geothermal Research 193 (1-2), 67–81.

Fee, D., Izbekov, P., Kim, K., Yokoo, A., Lopez, T., Prata, F., Kazahaya, R., Nakamichi, H., Iguchi, M., 2017. Eruption mass estimation using infrasound waveform inversion and ash and gas measurements: Evaluation at Sakurajima Volcano, Japan. Earth and Planetary Science Letters 480, 42–52.

Fee, D., Matoza, R. S., 2013. An overview of volcano infrasound: from hawaiian to plinian, local to global. Journal of Volcanology and Geothermal Research, 123–137.

Garcés, M., Harris, A., Hetzer, C., Johnson, J., Rowland, S., Marchetti, E., Okubo, P., 2003. Infrasonic tremor observed at K̄ilauea Volcano, Hawai'i. Geophysical Research Letters 30 (20), 1–4.

Gerst, A., Hort, M., Aster, R. C., Johnson, J. B., Kyle, P. R., 2013. The first second of volcanic eruptions from the Erebus volcano lava lake, Antarctica - Energies, pressures, seismology, and infrasound. Journal of Geophysical Research: Solid Earth 118 (7), 3318–3340.

Goto, A., Johnson, J. B., 2011. Monotonic infrasound and Helmholtz resonance at Volcan Villarrica (Chile). Geophysical Research Letters 38 (6), 1–5.

Hagerty, M. T., Schwartz, S. Y., Garcés, M. a., Protti, M., 2000. Analysis of seismic and acoustic observations at Arenal Volcano, Costa Rica, 1995-1997. Journal of Volcanology and Geothermal Research 101 (1-2), 27–65.

Ishihara, K., 1985. Dynamical analysis of volcanic explosion. Journal of Geodynamics 3 (3-4), 327–349.

Johnson, J., Aster, R., Jones, K. R., Kyle, P., McIntosh, B., 2008. Acoustic source characterization of impulsive Strombolian eruptions from the Mount Erebus lava lake. Journal of Volcanology and Geothermal Research 177 (3), 673–686.

Johnson, J., Ruiz, M., Ortiz, H. D., Watson, L. M., Viracucha, G., Ramon, P., Almeida, M., 2018a. Extraordinary Infrasound Tornillos Produced by Volcán Cotopaxis Deep Crater. Geophysical Research Letters, 1–9.

Johnson, J. B., 2003. Generation and propagation of infrasonic airwaves from volcanic explosions. Journal of Volcanology and Geothermal Research 121 (1-2), 1–14.

Johnson, J. B., Anderson, J., Marcillo, O., Arrowsmith, S., 2012. Probing local wind and temperature structure using infrasound from Volcan Villarrica (Chile). Journal of Geophysical Research 117.

Johnson, J. B., Miller, A. J. C., 2014. Application of the Monopole Source to Quantify Explosive Flux during Vulcanian Explosions at Sakurajima Volcano (Japan). Seismological Research Letters 85 (6).

Johnson, J. B., Palma, J. L., 2015. Lahar infrasound associated with Villarrica's March 3, 2015 eruption. Geophys. Res. Lett., 6324–6331.

Johnson, J. B., Watson, L. M., Palma, J. L., Dunham, E. M., Anderson, J. F., 2018b. Forecasting the eruption of an open-vent volcano using resonant infrasound tones. Geophysical Research Letters, 1–8.

Karlstrom, L., Dunham, E. M., 2016. Excitation and resonance of acoustic-gravity waves in a column of stratified , bubbly magma. Journal of Fluid Mechanics 797, 431–470.

Kim, K., Fee, D., Yokoo, A., Lees, J. M., 2015. Acoustic source inversion to estimate volume flux from volcanic explosions. Geophysical Research Letters (42).

Kim, K., Lees, J. M., 2011. Finite-difference time-domain modeling of transient infrasonic wavefields excited by volcanic explosions. Geophysical Research Letters 38 (6), 2–6.

Kim, K., Lees, J. M., 2014. Local Volcano Infrasound and Source Localization Investigated by 3D Simulation. Seismological Research Letters 85, 1–10.

Kim, K., Lees, J. M., Ruiz, M., 2012. Acoustic multipole source model for volcanic explosions and inversion for source parameters. Geophysical Journal International, 1192–1204.

Kinsler, L. E., Frey, A. R., Coppens, A. B., Sanders, J. V., 2000. Fundamentals of Acoustics, 4th Edition. John Wiley and Sons, New York.

Lacanna, G., Ripepe, M., 2013. Influence of near-source volcano topography on the acoustic wavefield and implication for source modeling. Journal of Volcanology and Geothermal Research 250, 9–18.

Lighthill, M. J., 1978. Waves in fluids. Cambridge University Press, Cambridge.

Marcillo, O., Johnson, J. B., Hart, D., 2012. Implementation, characterization, and evaluation of an inexpensive low-power low-noise infrasound sensor based on a micromachined differential pressure transducer and a mechanical filter. Journal of Atmospheric and Oceanic Technology 29 (9), 1275–1284.

Matoza, R. S., Fee, D., Garcés, M. a., Seiner, J. M., Ramón, P. a., Hedlin, M. a. H., 2009. Infrasonic jet noise from volcanic eruptions. Geophysical Research Letters 36 (8), 1–6.

Neal., C. A., Brantley, S. R., Antolik, L., Babb, J. L., Burgess, M., Calles, K., Cappos, M., Chang, J. C., Conway, S., Desmither, L., Dotray, P., Elias, T., Fukunaga, P., Fuke, S., Johanson, I. A., Kamibayashi, K., Kauahikaua, J., Lee, R. L., Pekalib, S., 2019. The 2018 rift eruption and summit collapse of K ī lauea Volcano. Science 363 (6425), 367–374.

Olson, H. F., 1957. Acoustical engineering. Van Nostrand Company, Princeton, New Jersey.

Oppenheimer, C., Kyle, P. R., 2008. Probing the magma plumbing of Erebus volcano, Antarctica, by open-path FTIR spectroscopy of gas emissions. Journal of Volcanology and Geothermal Research 177 (3), 743–754.
URL http://dx.doi.org/10.1016/j.jvolgeores.2007.08.022

Palma, J. L., Calder, E. S., Basualto, D., Blake, S., Rothery, D. A., 2008. Correlations between SO2 flux, seismicity, and outgassing activity at the open vent of Villarrica volcano, Chile. Journal of Geophysical Research: Solid Earth 113 (10), 1–23.

Richardson, J. P., Waite, G. P., Palma, J. L., 2014. Varying seismic-acoustic properties of the fluctuating lava lake at Villarrica volcano, Chile. Journal of Geophysical Research: Solid Earth, 1–14.

Ripepe, M., Marchetti, E., Bonadonna, C., Harris, A. J. L., Pioli, L., Ulivieri, G., 2010. Monochromatic infrasonic tremor driven by persistent degassing and convection at Villarrica Volcano, Chile. Geophysical Research Letters 37 (15), 2–7.

Ripepe, M., Poggi, P., Braun, T., Gordeev, E., 1996. Infrasonic waves and volcanic tremor at Stromboli. Geophysical Research Letters 23 (2), 181–184.

Rossing, T. D., Fletcher, N. H., 2004. Principles of Vibration and Sound, 2nd Edition. Vol. 1. Springer.

Rowe, C. A., Aster, R. C., Kyle, P. R., Dibble, R. R., Schlue, J. W., 2000. Seismic and acoustic observations at Mount Erebus Volcano, Ross Island, Antarctica, 1994-1998. Journal of Volcanology and Geothermal Research 101 (1-2), 105–128.

Spina, L., Cannata, A., Privitera, E., Vergniolle, S., Ferlito, C., Gresta, S., Montalto, P., Sciotto, M., 2014. Insights into Mt. Etnas Shallow Plumbing System from the Analysis of Infrasound Signals, August 2007December 2009. Pure and Applied Geophysics 172 (2), 473–490.

Svärd, M., Nordström, J., 2014. Review of summation-by-parts schemes for initial-boundary-value-problems. Journal of Computational Physics 268, 17–38.

Van Daele, M., Moernaut, J., Silversmit, G., Schmidt, S., Fontijn, K., Heirman, K., Vandoorne, W., De Clercq, M., Van Acker, J., Wolff, C., Pino, M., Urrutia, R., Roberts, S. J., Vincze, L., De Batist, M., 2014. The 600 yr eruptive history of Villarrica Volcano (Chile) revealed by annually laminated lake sediments. Bulletin of the Geological Society of America 126 (3-4), 481–498.

Vergniolle, S., Brandeis, G., 1996. Strombolian explosions: 1. A large bubble breaking at the surface of a lava column as a source of sound. Journal

of Geophysical Research 101 (B9), 20433.

Vergniolle, S., Brandeis, G., Mareschal, J., 1996. Strombolian explosions 2: eruption dynamics determined from acoustic measurements. Journal of Geophysical Research 101 (B9), 20449–20466.

Vidal, V., Géminard, J. C., Divoux, T., Melo, F., 2006. Acoustic signal associated with the bursting of a soap film which initially closes an overpressurized cavity: Experiment and theory. European Physical Journal B 54 (3), 321–339.

Witsil, A. J., Johnson, J. B., 2018. Infrasound explosion and coda signal investigated with joint analysis of video at Mount Erebus, Antarctica. Journal of Volcanology and Geothermal Research 357, 306–320.
URL https://doi.org/10.1016/j.jvolgeores.2018.05.002

Witter, J. B., Kress, V. C., Delmelle, P., Stix, J., 2004. Volatile degassing, petrology, and magma dynamics of the Villarrica Lava Lake, Southern Chile 134, 303–337.

Woulff, G., McGetchin, T. R., 1976. Acoustic noise from volcanoes - Theory and experiment.

Yamada, T., Aoyama, H., Nishimura, T., Iguchi, M., Hendrasto, M., 2017. Volcanic eruption volume flux estimations from very long period infrasound signals. Geophysical Research Letters 44 (1), 143–151.